



A mechanistic study of the interactions between methane and nickel supported on doped ceria

Mengzheng Ouyang^a, Paul Boldrin^{a,*}, Robert C. Maher^b, Xiaolong Chen^c, Xinhua Liu^c, Lesley F. Cohen^b, Nigel P. Brandon^a

^a Department of Earth Science and Engineering, Imperial College London, London, SW7 2BP, United Kingdom

^b The Blackett Laboratory, Imperial College London, London, SW7 2BZ, United Kingdom

^c Dyson School of Design Engineering, Imperial College London, London, SW7 1AL, United Kingdom



ARTICLE INFO

Keywords:

Partial oxidation of methane (POM) catalyst
In-situ Raman spectroscopy
Nickel/gadolinium-doped ceria
Solid oxide fuel cell (SOFC)
Chemical looping combustion (CLC)

ABSTRACT

A novel combined method using modified methane pulses and in-situ Raman spectroscopy together with mass spectrometry is applied to impregnated Ni/gadolinium-doped ceria (CGO). The partial oxidation of methane is deduced to proceed via a Mars-van-Krevelen type mechanism composed of initial methane decomposition together with carbon oxidation by oxygen from CGO. The critical role of the ceria surface and the bulk oxygen in the reaction is defined in detail. Oxygen is a necessary reactant in the reaction, as well as inhibiting carbon deposition. Oxygen spill-over is the driving force for the carbon oxidation and the ceria surface oxygen is resupplied by bulk oxygen after depletion. Bulk migration of oxygen to the surface is the rate-determining step. We also demonstrate that the ceria oxygen stoichiometry significantly affects the type of reaction and the rate of reaction between methane and Ni/CGO: The total oxidation of methane happens only when the oxygen stoichiometry is high while the oxygen spill-over rate decreases with decreasing oxygen stoichiometry, which reduces the rate of carbon elimination and results in reduction in the rate of methane oxidation. This work lays out a comprehensive evaluation methodology and provides important insights for future design of methane oxidation catalysts for solid oxide fuel cells, and more widely for methane reforming with different oxidants (steam, CO₂, NO₂ etc.).

1. Introduction

Catalysed reactions involving methane and other hydrocarbons are amongst some of the most important in the chemicals industry, for example methane steam reforming is currently used to generate 96% of the hydrogen produced in the world [1]. Because production of hydrogen by methane reforming is likely to be lower carbon than electrolysis for a considerable period of time, any move towards a “hydrogen economy” is likely to require a large increase in the amount of methane reforming. Because of this, alternatives such as catalytic partial oxidation of methane [2,3] and chemical looping combustion/reforming (CLC/CLR) are being researched, while solid oxide fuel cells (SOFCs) running directly on methane may potentially negate the need for reforming. Because of its high activity towards C–H scission process, nickel is the most studied non-noble metal catalyst for catalytic conversion of methane [4–6]. However, Ni is also highly susceptible to carbon deposition [7]. Supports which feature a multivalent metal ion have been found to be effective in reducing carbon deposition [8], and

some of the most widely used are ceria and doped ceria, where some of the cerium is able to switch between the +3 and +4 oxidation states. In particular, ceria doped with lower valence metals offers the advantage of a high oxide ion mobility [9] and the ability of the structure to tolerate a substantial degree of ceria reduction before changes in the crystal structure occur [10]. These features make Ni/ceria an ideal oxygen carrier for the CLR process [11] and also a promising anode in solid oxide fuel cells (SOFCs), which are able to run on carbon-containing fuels. Doped ceria has been shown to reduce carbon deposition in SOFC electrodes. The most widely used doped ceria in SOFCs is gadolinium-doped ceria (cerium-gadolinium oxide, CGO) due to the higher oxide ion conductivity brought by doping. In CLR, it was also found that the active particles supported on CGO were more reactive compared to those supported on undoped ceria [12]. In both CLR and SOFC systems, oxidation of methane on Ni/ceria happens in an oxygen free condition, which further aggravates its vulnerability towards carbon deposition. Therefore, it is very important to understand the mechanism of partial oxidation of methane (POM) and carbon

* Corresponding author.

E-mail address: p.boldrin@imperial.ac.uk (P. Boldrin).

deposition in oxygen free conditions, especially the relationship between mechanism and oxidation state of ceria.

On an inert support, the partial oxidation of methane tends to take place via a Langmuir-Hinschelwood mechanism where oxygen and methane are chemisorbed on the surface of the metal [13] but on an active support such as ceria, a Mars-van Krevelen mechanism becomes possible, where the hydrocarbon chemisorbs on the metal while other species chemisorb on the support. This mechanism introduces extra steps into the reaction as one of the species has to spill over onto the other phase, or alternatively the reaction may take place at the boundary between the metal and support. This has been observed experimentally with well-defined model catalysts [14].

Much work has been done on Ni/ceria catalysts to explore activity–structure relationships, mostly done by steady-state approaches [15–17], which are facile and readily scaled up to industrial scale. However, steady-state approaches suffer from several intrinsic disadvantages: 1. The kinetic data of steady-state approaches is usually related to only the rate determining step and does not provide detailed information of a complex multi-step process such as catalytic oxidation of methane [18]. 2. The observed kinetic data corresponds with factors other than structure of catalyst, such as gas composition, time of reaction. Therefore, detailed activity–structure relationships are difficult to be established using steady-state kinetic data.

Transient studies can generate a perturbation in the system and then the relaxation/response of the system is monitored. Therefore, some short-lived intermediate species that are not seen in steady-state approaches can be investigated [19]. Transient methods have been widely applied on ceria-based catalysts to determine the oxygen storage capacity (OSC) [20,21] or to investigate the mechanism of methane catalysis [22,23]. Although in these works the kinetic data were well-interpreted quantitatively, the qualitative information such as shape and broadening of peaks that can also provide information related to reaction mechanism more intuitively were somewhat overlooked. In the literature on solid state chemistry, transient experiments such as electrical conductivity relaxation [24,25] and gravimetric relaxation [26,27] have been used to measure parameters such as the chemical diffusion coefficient (D_{chem}) and the surface exchange coefficient (k_s) over a wide pO_2 range but these experiments need certain geometries of samples, custom-designed equipment and are not appropriate for studying real electrode or catalyst structures.

On the other hand, transient methods have not been applied on any attempt aiming at relating the carbon resistance of Ni/CGO with its intrinsic properties which is of much importance in industrial processes like catalytic partial oxidation or steam reforming of methane (POM, SRM), and actual application of SOFC and CLR on methane fuel. In different conditions the catalyst will be at a different equilibrium state depending on the gas composition (for example the steam/carbon ratio) and the composition of the catalyst (for example the level of doping of the support or active metal). These different equilibrium states could mean differences in parameters which may affect the performance of the catalyst, such as the surface coverage of carbon or the oxidation state of the bulk and the surface of the catalyst support. As a simple example, the energy of a surface oxygen atom on CeO_2 will be different to the energy of a surface oxygen atom on $\text{CeO}_{1.95}$, and this will change the rates of certain steps of the reaction. The effect of this on the performance of ceria and doped-ceria catalysts has not yet been investigated. Work to fill in the gap on a real-life catalyst environment is therefore a pressing need.

In this paper we use a facile methane transient pulse experiment in ambient pressure condition rather than vacuum condition to avoid the pressure gap [19,28]. Combined with in-situ Raman spectroscopy, the catalytic partial oxidation of methane in oxygen free conditions was investigated. By a combination of quantitative and qualitative analysis of the results, it is found that the methane partial oxidation mechanism on a Ni/CGO catalyst is indeed Mars-van Krevelen, and that the reaction is limited by the migration of oxygen through the bulk of the

support. The rate of reaction, carbon resistivity and CO selectivity change with oxygen stoichiometry is also studied, and this provides insights on catalyst design for SOFC anodes and the CLR process, as well as providing a way to evaluate the performance of catalyst systems for oxidation of hydrocarbons within a realistic real-use scenario.

2. Experimental

2.1. Sample preparation

The Ni/CGO sample was prepared via the tape casting and impregnation method in order to produce a microstructure similar to an SOFC electrode in a powder form. At first, a CGO ink was prepared by mechanically mixing commercial gadolinium doped ceria ($\text{Gd}_{0.9}\text{Ce}_{0.1}\text{O}_{1.95}$, Praxair, particle size = 0.5 μm) with carbon black as a pore former, Hypermer KD15 as a dispersant and an ethylcellulose binder (Hercules EC N-7) in a triple roll mill. Secondly, the ink was tape cast onto an alumina plate followed by calcination in a muffle furnace (Elite Co.) at 1350 °C. Thirdly the calcined sample was scraped down from the plate and ground. Then the powder with total weight of 1 g was impregnated with 2 M $\text{Ni}(\text{NO}_3)_2 \cdot 6\text{H}_2\text{O}$ (Sigma-Aldrich) ethanol solution, the impregnation was conducted as follows: 4 μL of solution was dropped onto the sample along with grinding in the mortar to acquire uniformity; Then the powder was calcined in a muffle furnace at 500 °C for 30 min to convert $\text{Ni}(\text{NO}_3)_2 \cdot 6\text{H}_2\text{O}$ to NiO . After that the powder was weighted on an analytical balance to determine the actual amount of NiO introduced, and the nickel amount after reduction was calculated accordingly. The above process was repeated until the amount of nickel reached more than 20 wt% (21.3 wt% after the last impregnation). After impregnation, the sample was further calcined at 800 °C for 4 h.

Commercial Ni/YSZ and Ni were provided by Fuel Cell Materials. The Ni/CGO and Ni/YSZ had metal loadings of 54.1 wt% and 61.7 vol% NiO respectively, with a NiO particle size of 500–1000 nm.

2.2. Powder characterization

2.2.1. Morphology and crystallinity

The morphology of Ni/CGO powder was characterized by SEM (Leo 1530 Gemini, Zeiss), crystallinity and crystal size were characterized by XRD (X'Pert³ Powder, Malvern Panalytical). Sample surface area was characterized by BET (ASAP 2460, Micromeritics).

2.2.2. Catalytic property

The catalytic property of powder was examined using a catalyst characterization system (AutoChem II 2920, Micromeritics). The powder sample was placed on a piece of quartz wool inside a U-shaped quartz tube. The composition of outlet gas was analyzed using a mass spectrometer (Cirrus 2 Quadrupole Mass Spectrometer, MKS). A series of temperature programmed procedures were used to analyse the morphology and reactivity with methane. The sample was first reduced in a temperature programmed reduction procedure (TPR), the temperature was raised to 600 °C with 5 °C/min ramping rate in 50 mL/min 20% H_2/Ar mixing gas. H_2 (amu 2) and H_2O (amu 18) were monitored in the mass spectrometer. In a methane pulse (MP) experiment, 0.3793 mL of methane was injected into 0.1 g of 20 wt% Ni/CGO sample at 600 °C in each pulse, followed by flushing of 50 mL/min of Ar during the pulse interval, the pulse number and time of interval were adjusted as variables. The injection is performed by an automatic injector in the AutoChem II 2920 catalyst characterization system. CH_4 (amu 15), CO (amu 28), CO_2 (amu 44), H_2 (amu 2), and H_2O (amu 18) were monitored in a mass spectrometer. MP was performed in two ways. First a series of pulses with different intervals were performed to investigate the difference when changing interval and pulse numbers. 30 pulses were injected when the interval was 10 min, and 15 pulses were injected when interval was 30 min or 90 min. Commercial

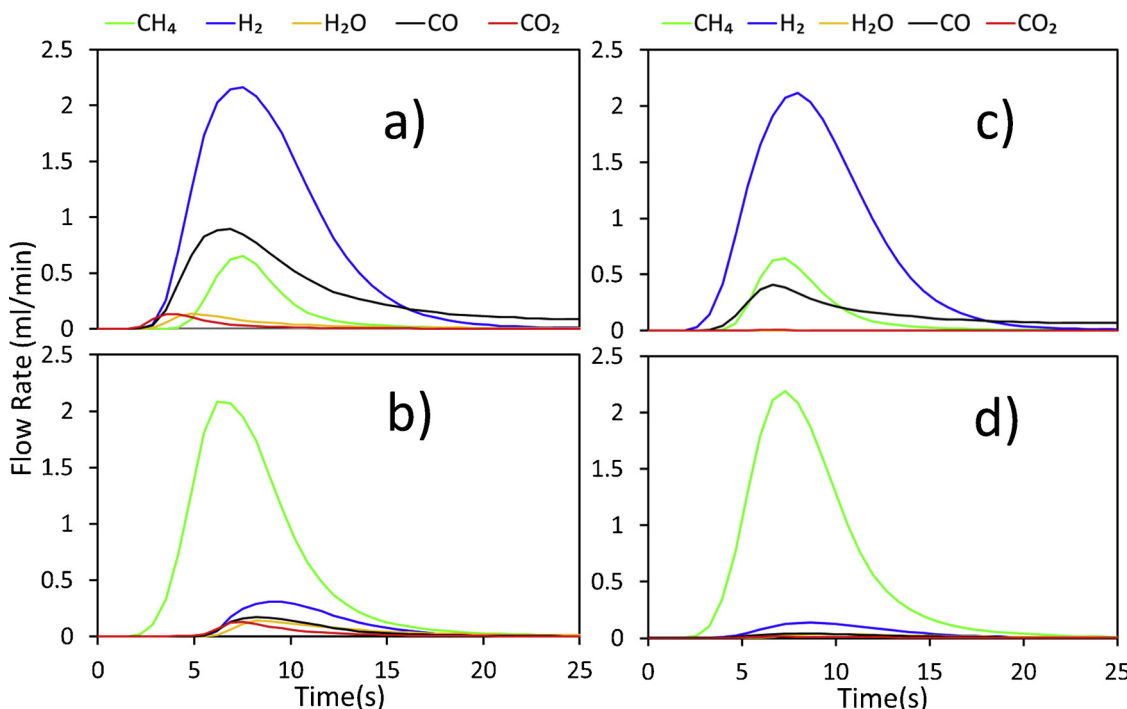


Fig. 1. The products of the first and second methane pulses in methane pulse with 30 min interval. First pulse on a. Ni/CGO; b. CGO. Second methane pulse on c. Ni/CGO; d. CGO. The y axis is the flow rate of each species in ml/min CH_4 (amu 15), H_2 (amu 2), H_2O (amu 18), CO (amu 28) and CO_2 (amu 44) are monitored.

powders of Ni/YSZ and Ni were used to provide a comparison. As a final step, temperature programmed oxidation was performed to investigate the form of carbon deposition in each methane pulse experiment. 50 mL/min 2% O_2/Ar mixing gas was used in the oxidation with the temperature raised to 1000 °C at a 5 °C/min ramping rate. Ar (amu 40), O_2 (amu 32) and CO_2 (amu 44) were monitored in the mass spectrometer.

Methane pulse with water reoxidation experiments were performed on impregnated Ni/CGO powder. 0.2326 mL methane were injected at 15 min intervals. Every seven methane pulses, pulses of 0.2326 mL 12.3 vol% $\text{H}_2\text{O}/\text{Ar}$ were injected with an interval of 0.5 min until no hydrogen production was observed. This indicates that ceria was oxidised to a certain oxidation state. CH_4 (amu 15), CO (amu 28), CO_2 (amu 44), H_2 (amu 2), and H_2O (amu 18) were monitored in a mass spectrometer.

Calibration was performed before the recording of each methane pulse experiment. The process of calibration is as follows: Pulse a known volume V' of standard gas or gas mixtures (H_2 , CH_4 , 1% CO/Ar) through the mass spectrometer and the signal shown is $I'(t)$. Then in the real methane pulse experiment, the volume of this type of gas V can be derived from $V = \frac{V'}{\int_0^t I'(t) dt}$, in which the $I(t)$ is the signal of mass spectrometer on this type of gas in real methane pulse experiment. The mass spectrometer data was analyzed by OriginLab 8.6.

2.3. Raman spectroscopy

In-situ Raman measurements were carried out using a Jobin-JBvon LabRam HR-1000 confocal microscope. Spectra were collected using a 514 nm Argon ion laser which was focused onto the sample using a $\times 20$ long working distance objective. This resulted in a spot with a diameter of approximately 4 μm at the focal point. The incident laser power and integration times used for the measurements were optimized before for each to ensure a good signal-to-noise ratio was achieved while any possible laser heating was minimized. Integration times varied between 5 and 15 s and the laser intensity was constant at approximately 4 mW at the focal point. An schematic indication of in-situ

Raman setup is shown in Fig. S6.

In-situ Raman spectra were collected from the samples in real time using a high temperature catalytic stage from Linkam Scientific. Raman spectra were collected at 600 °C as reported by the stage controller. Continuous flows of N_2 and H_2 were delivered to through the stage to the samples using a system of calibrated mass flow controllers. Samples were prepared by reducing using a mixture of 90% N_2 : 10% H_2 for at least an hour and then purged at temperature for 12 h in pure N_2 in order to minimize the presence of any water in system. All gas mixtures passed through the system at a total rate of 100 mL/min.

During the experiment, 100 mL/min Ar passed through 0.1 g impregnated Ni/CGO powder and 0.3793 mL methane was injected manually through a Rheodyne 7010 injector every 20 min. H_2 , CO, CH_4 , CO_2 and H_2O were monitored by a Thermo Fisher ProLab Benchtop Mass Spectrometer at the same time.

All Raman spectra collected were analyzed using a combination of the JY LabRam software, Peakfit v4 and OriginLab 8.6. Spectra were normalized to their total intensity in order to compensate for any differences in focal conditions. They were then background corrected and fitted to Voigt modes using Peakfit v4 or integrated over regions of interest using OriginLab. The resulting data was then further analyzed using OriginLab 8.6.

3. Results and discussion

3.1. Methane pulse experiments

3.1.1. The first two pulses

From initial characterisations of the sample with XRD and SEM, the particle size of nickel is ~20 nm, gadolinium-doped ceria (CGO) ~100 nm (Fig. S1), while the surface area of unimpregnated CGO powder indicated by BET is 13.85 m^2/g . The nickel surface area was estimated by the nickel particle size as 3.03 m^2/g , assuming all nickel formed 20 nm semi-spherical particles on CGO.

Before the methane pulse, the 0.1 g powder sample first went through a TPR in 50 mL/min 10% H_2/Ar to 600 °C with ramping rate of 5 °C/min to reduce NiO to Ni. All NiO was reduced to Ni as seen in the

TPR result in Fig. S2a. Then it was flushed at 600 °C by 50 mL/min Ar for 2 h to ensure all H₂ and H₂O desorbed from Ni/CGO surface. During the methane pulse experiments, a loop valve is used to pass 0.3793 mL of pure methane (equivalent with 169.3 μmol/g) over the sample at 600 °C.

When the sample is Ni/CGO, the methane reacts with the surface producing a mixture of CO₂, CO, H₂ and H₂O (Fig. 1a). The signal of the mass spectrometer is proportional to the partial pressure of the monitored gas species and the relative intensity of different mass of such gas species, the signal was calibrated and converted into a production rate (ml/min). An identical experiment using only CGO as the sample showed much lower conversion of methane (Fig. 1b), confirming that the nickel is the main point of interaction with the methane. Interestingly, in this first pulse the main reaction on Ni/CGO was partial oxidation of methane (POM) producing CO and H₂ with a molar ratio of ~1:2, and the amount of the converted methane reacting through the total oxidation of methane (TOM) producing CO₂ and H₂O with a molar ratio of ~1:1 is small (< 20%), while on pure CGO ca. 40% of the reacted CH₄ was converted to CO₂ and H₂O by TOM. On Ni/CGO, CO₂ and H₂O were detected by the mass spectrometer earlier than CH₄, CO and H₂. This is not observed on CGO, suggesting the total oxidation of methane on Ni/CGO is a direct oxidation step, rather than further oxidation of CO and H₂. It may suggest that the source of the oxygen for TOM on these two samples are at different sites; on CGO the reaction involves surface oxygen, while on Ni/CGO it is either oxygen spilled-over to nickel [29] or oxygen at the interface between nickel and CGO [30]. It has been widely found that Ni supported on CGO is partly covered by oxygen spilled over from CGO [31–33]. In both cases, the concentration of all gases drops to background levels within 30 s.

Because the methane reacting with the surface of the sample causes an oxygen gradient in the sample and possible carbon deposition, after the pulse a period of time was allowed for the sample to reach equilibrium before another pulse of methane was passed over the sample. The following results in this section are all from methane pulse with a 30 min interval between pulses (10 min, 30 min and 90 min interval methane pulse experiments were performed and are included in supplementary information Fig. S3a-c). In this second pulse the CO₂ production fell by 80% in both samples (Fig. 1c and d), while by the third pulse there was negligible CO₂ production suggesting that the TOM process requires oxygenated sites on the surface of CGO and Ni, since the CGO becomes more reduced with each pulse. This is in accordance with Chin [34], who found that reaction between methane and oxygen chemisorbed on metal would preferably produce CO₂, and CO was produced only when oxygen coverage was extremely low. This in turn suggests that by the third pulse the oxygen coverage on nickel surface is extremely low.

3.1.2. Subsequent pulses

Starting from the second pulse, it becomes clear that CO is still being produced for a period of time after all the other gases have exited the reactor (Fig. 2a). Identical experiments with either no sample (only methane is observed, as shown in Fig. S3) or with Ni impregnated YSZ (Fig. 2a) showed no such behaviour, indicating that it is not the result of a slow desorption of gaseous CO from the reactor or the nickel nano particles in the sample (the complete result of the methane pulse experiment with 30 min interval on Ni/YSZ is shown in Fig. S4 in SI). This leaves the reaction of carbonaceous species on the nickel surface with oxygen from the CGO as the likeliest explanation. With subsequent pulses, this tail of CO production becomes longer, eventually reaching over 30 min. Whatever reaction is producing the CO is becoming slower as the CGO becomes more reduced.

In these later pulses, the CO production can be divided into two phases – the initial peak coincident with the other species from the methane pulse, and the tail which continues after all the other gas species have fallen to background levels. The shapes of the two peaks suggest these are two oxidation processes. In all the pulses from the

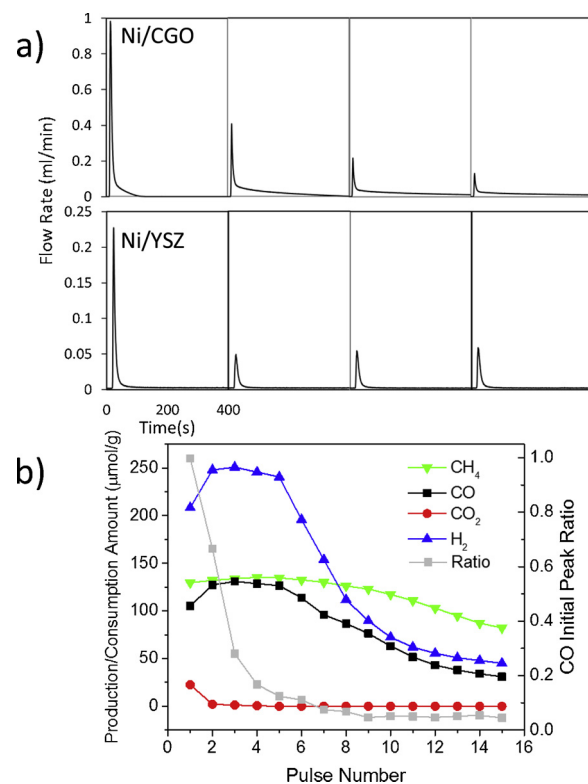


Fig. 2. Evolution of CO peak shape with increasing pulse number in methane pulse with 30 min interval. a. The first to fourth CO production peak of a methane pulse on Ni/CGO and on Ni/YSZ. For Ni/CGO, from the second methane pulse, CO production peak consists of an initial peak and a tail, the length of tail extends with pulsing number. This is not observed in Ni/YSZ. Y axis is mass spectrometer signal intensity. b. Red, green and black lines are the amount of CO and CO₂ produced, and CH₄ consumed, in each methane pulse; the grey line is the proportion of CO produced in initial peak versus the total CO produced in each methane pulse. (For interpretation of the references to colour in this figure legend, the reader is referred to the web version of this article).

second pulse onwards, and before the tail overlapped with the next pulse (fifth pulse), the total amount of CH₄ consumed and CO produced remains constant within the range of error (< ± 2%) (Fig. 2b), despite the massive change of the peak shape. The ratio of the CO amount in the initial peak to the amount in the tail is depicted in Fig. 2b, it decreases with number of pulses. This suggests that the two processes are competing with each other and involve a reaction on nickel sites. The spill-over of oxygen onto metal sites from doped ceria has been widely observed previously [14,32,35]. Due to the oxygen deficiency on nickel surface, the oxygen for CO production can only come from the lattice oxygen of CGO. It is likely that the initial peak is methane cracking at the surface of nickel with any deposited carbon species (C/CH_x) being oxidized by the surface oxygen from CGO. The tail is caused by oxidation of the deposited carbon species by oxide ions migrating from the bulk of CGO after the surface oxygen is depleted (the Mars-van Krevelen mechanism). When the tail of CO production overlaps with the next pulse at the fifth pulse, this means that at the time of the fresh injection of methane, it is likely that there is still carbon remaining on the surface of the nickel from the previous pulse, blocking the reactive sites. Because of this, the consumption of methane and the production of CO decrease after the fifth pulse. This deduction is further proved by methane pulse with 90 min interval (as shown in Fig. S3c), in which the CO tailing did not reach the next injection during all 15 pulses. The consumption and production of all species remained constant after the first few pulses whereas these are changing with number of pulses in the 30 min interval experiment shown in Fig. 2a, suggesting the tailing is oxidation of carbon species deposited on Ni.

Temperature-programmed oxidation (TPO) experiments following these methane pulse experiments show that there is no carbon deposition on the sample, as long as enough time has been left between pulses to allow the concentration of CO to drop to baseline levels. For example, at high oxidation states carbon can be eliminated within 20 s, while after the second methane pulse the carbon elimination time increases to 100 s. As the CGO oxidation state decreases, the time required can increase to 60 min. In methane pulse with 90 min interval, the CO tailing did not extend to the next pulse during the whole duration, and no carbon is detected in subsequent TPO, as opposed to TPO after 10 min and 30 min interval methane pulse experiment (The TPO results of methane pulse with different intervals is included in supplementary document Fig. S2b). Conversely, if not enough time is left between pulses (i.e. if CO is still being detected at the time of the next pulse of methane) then there is carbon deposition detected by subsequent temperature-programmed oxidation (TPO) experiments (Fig. 4a). Even if some pulses have overlapped, if enough time is left after the final pulse then no carbon is detected by TPO.

These observations strongly suggest that the initial carbon deposition is fully reversible on metal-CGO based catalysts if there is still reducible CGO present. The carbon deposits are oxidized at a low temperature of 450 °C in the TPO measurement, compared with other's work, in which highly amorphous carbon is oxidized at ~530 °C and graphitic carbon at 650 °C [36]. This suggests that carbon deposits caused by the methane pulses are in more disordered form, likely in the form of clusters made only of several atoms, as reported by Hofmann to be the initial stage of carbon formation [37]. Amorphous carbon resulting from methane reforming was oxidized at ~600 °C [38], which further suggests that the carbon deposition here was not agglomerated. Since methane cracking on nickel would readily result in crystallized carbon (graphite for example) [39], these observations suggest that when carbon deposits at a rate which is faster than oxygen can be supplied, then carbon would aggregate on nickel and with increasing carbon concentration would turn from dispersed clusters to aggregated amorphous carbon, and finally to graphitic carbon.

To confirm these hypothesis, in-situ Raman was performed.

3.2. In-situ Raman experiments

Fig. 3a inset shows the Raman spectrum of the impregnated Ni/CGO sample obtained in-situ at 600 °C after it had been reduced in hydrogen. A complete Raman spectrum as a function with time is shown in SI (Fig. S7). The sharp peak at approximately 450 cm⁻¹ is the main F_{2g} Raman peak of CGO which corresponds directly to the Ce^{IV}-O bond [16]. The small shoulder observed at approximately 600 cm⁻¹ arises due to oxygen vacancies within the lattice caused by both the doping of the ceria with Gd and the partial reduction of Ce⁴⁺ to Ce³⁺ [40,41]. The broad peak at 900-1330 cm⁻¹ is the second order mode of the Ce^{IV}-O vibration peak (centred at ca. 1180). Ordinarily the NiO 2 P peak would also be located in the same position (centred at ca. 1070 cm⁻¹) [42], the 2 M peak should located at ca. 1500 cm⁻¹. However here we did not observe any extra peak at these two locations, suggesting that very little NiO should be present after reduction. The main F_{2g} peak is a direct indication of the percentage of Ce^{IV} at the sample surface (determined by the penetration depth of Raman laser) relative to the initial state during monitoring. As a result, the relative oxidation state of the CGO surface can be monitored in-situ and in real time using the integrated intensity of the F_{2g} peak.

In methane pulse experiment monitored by in-situ Raman, 0.3793 mL methane was injected into the sample every 20 min, with 50 mL/min pure Ar flushing during the intervals. Four gas species were monitored using the mass spectrometer: H₂, CH₄, CO, and CO₂, the production and consumption amount of which are plotted in Fig. 3b. The integrated intensity of the F_{2g} Raman peak was monitored during the methane pulse experiment and the integrated intensity is plotted in Fig. 3a along with the CO signal from mass spectrometer. TPO was

performed on the Ni/CGO sample after pulse experiments to examine any carbon deposition.

The result of the mass spectrometry test was similar to previous methane pulse experiments. POM was the major reaction as well although a considerable amount of CO₂ and H₂O were produced in the first 2 pulses. It is probably because the sample was slightly oxidized from the trace oxygen in the environment as the chamber was flushed in argon flow for 12 h at 110 °C. A CO tail appeared from the second pulse and extended with the number of pulses. The total production of CO was identical in the second to fourth pulse, and from the fourth pulse the CO tail extended longer than the interval time (20 min) and CO production reduced. The change in the amount of H₂ produced was similar to that of CO.

The integrated intensity of the F_{2g} peak decreased sharply immediately after each methane pulse, then gradually recovered during the interval. As the number of pulses increased, the rate of recovery decreased significantly, and the intensity of F_{2g} peak was recovered to a lower level. Although TPO showed that there was carbon deposition on Ni/CGO after the methane pulse experiments (Fig. S2b), no peak of carbon was observed in the Raman spectra during the whole pulse experiment, which would normally appear as two peaks, the D and G at 1350 cm⁻¹ and 1580 cm⁻¹ respectively [43,44], suggesting the carbon deposition amount was below the detection limit of Raman spectrometer.

While the significant drop of the F_{2g} peak intensity after each pulse was observed in experiments on Ni/CGO, on CGO the reduction of the peak intensity was much smaller (supplementary information Fig. S6). This indicates that the near surface oxygen of CGO was consumed immediately by the pulse, confirming that major CO peak is caused by the oxidation of surface C/CH_x species by CGO surface oxygen. The recovery of the Raman peak shows the surface oxygen was resupplied by bulk oxygen of CGO, which slows down with pulse numbers, by the decreases of oxygen migration rate from decreasing CGO oxygen stoichiometry.

After the third pulse on Ni/CGO, instead of instant recovery, the F_{2g} peak maintained at a plateau at a low level for ~16 min, then starts to recover. The mass spectrometry data showed the CO tail on the third pulse faded to the baseline value at almost the same time. This suggests that after the pulse, surface oxygen level was suppressed as oxygen migrating from bulk CGO preferentially spills-over to the nickel surface to react with carbon species. After all the carbon is removed, oxygen from the bulk of CGO remains on the surface of the CGO and results in the acceleration of the recovery of the F_{2g} peak. It is safe to conclude that the rate-determining step of carbon removal on Ni/CGO in oxygen free conditions is the bulk migration of oxygen: O_{Bulk} → O_{Surface}.

Note that Raman spectroscopy shows the surface CGO oxidation state has recovered to a low level after a sudden drop at the injection of methane, and maintained at this level as carbon species are being oxidized by oxygen migrated from bulk CGO (CO tail). At this stage, there is still available oxygen on the CGO surface, whose concentration c_{OSurface} is in dynamic equilibrium under the effect of source (O_{Bulk} → O_{Surface}) and sink (O_{Surface} → O_{Ni} + C* → CO*). The migration rate of the source decreases with decreasing CGO oxidation state, therefore the carbon oxidation rate slows down. If another pulse of methane comes through before all the carbon species are oxidized, it causes a sudden increase of carbon species on Ni surface, and thus pushes the equilibrium of the sink process towards product and causes a sudden decrease of c_{OSurface}. The detailed kinetics of this process is beyond the reach of this work but will be investigated in the future.

The combination of in-situ Raman and mass spectrometry provides direct evidence of the nature of the reaction of CH₄ on Ni/CGO in oxygen free conditions, proving that methane was first adsorbed and decomposed on nickel before being oxidized by oxygen migrated from the surface of the CGO. Bulk oxygen from CGO then migrates to the surface to fill the vacancy. It also indicates that oxygen migration from bulk CGO to the surface is the rate-limiting process in carbon

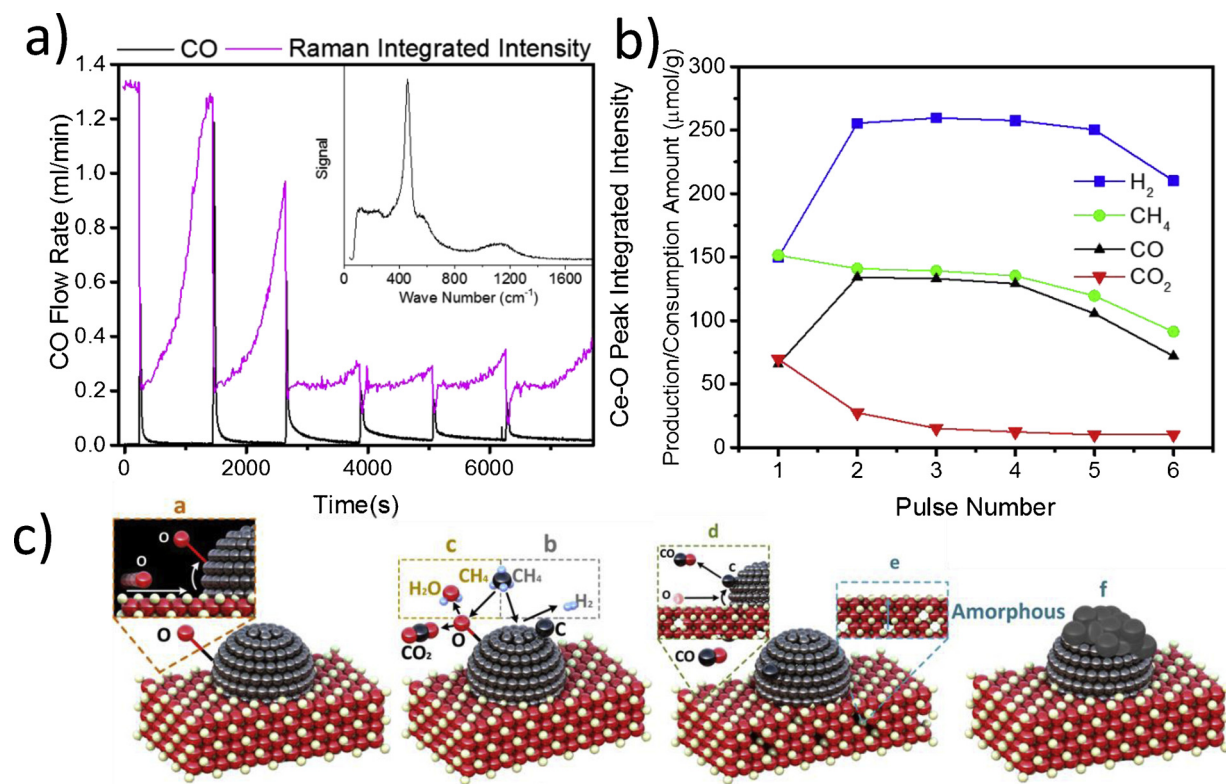


Fig. 3. In situ Raman methane pulse experiments a) CO signal from the mass spectrometer (black line) and integrated Ce^{IV}-O F_{2g} peak intensity (purple line) with time (inset is the Raman spectrum for reduced Ni/CGO sample); b) Production/consumption amount of gas species in the methane pulse experiment with in-situ Raman by mass spectrometer vs. pulse number; c) Proposed mechanism for methane oxidation in given condition: Methane either decomposes at the surface of CGO or reacts with adsorbed oxygen, then carbon species are oxidized by oxygen spilled-over from the CGO surface; after depletion of surface oxygen, oxygen from the bulk CGO migrates to the surface; If carbon is not oxidized, it will accumulate and form amorphous and eventually crystallized carbon deposits. (For interpretation of the references to colour in this figure legend, the reader is referred to the web version of this article).

elimination.

From the preceding conclusions, a mechanism for the reaction can be derived (H₂, CO and CO₂ desorption in step b, c and d are rapid at 600 °C and so have been omitted [45,46], the methane dehydrogenation process the detailed reaction steps of CH_x with O* involving CHO* is also omitted here because it is generally believed to be very fast, and it is shown in the methane pulse experiment that no hydrogen was produced after the major peak of CO. The detailed reaction route of TOM is also omitted for the same reason):

- a $O_{CGO}^{surface} \rightarrow O_{Ni}^*$
- b $CH_4(g) + S_{Ni}^* \rightarrow C + 2H_2(g)$
- c $CH_4(g) + 4O_{Ni}^* \rightarrow CO_2(g) + 2H_2O(g)$
- d $O_{CGO}^{surface} \rightarrow O_{Ni}^* + C \rightarrow CO(g)$
- e $O_{CGO}^{bulk} \rightarrow O_{CGO}^{surface}$
- f $C_{Ni}^* \rightarrow C_{amorphous}$

As shown in Fig. 3c, the process of methane oxidation on Ni/CGO consists of five elementary steps: methane cracking at the surface sites of nickel; methane total oxidation by adsorbed oxygen on the nickel surface; oxygen migration across the CGO surface and spill-over to the nickel surface; oxygen reaction with adsorbed carbon species; oxygen migration from bulk to surface CGO. Surface migration and spill-over of oxygen is generally believed to be very fast compared with bulk diffusion (10⁵ times faster according to Holmgren's work [47]). The reaction between adsorbed carbon species and oxygen spilled-over from CGO is fast compared with methane dehydrogenation according to literatures [5,48]. In this work, the dehydrogenation of methane in each pulse is completed in the major peak less than 20 s after the pulse was injected, as can be seen by the fact that there is no hydrogen production after the initial pulse, while the length of the CO production tail ranged

from 30 s to 30 min after the major peak, indicating that the reaction between surface carbon and oxygen is not the rate-limiting step of subsequent carbon oxidation. Therefore, it is reasonable to conclude the rate determining step is oxygen migration from bulk to surface CGO. According to Chin's work, at $pO_2/pCH_4 < 0.08$ methane is deduced to mainly activate at empty sites of metal catalysts, without the participation of oxygen [34]. In our case, sample is reduced in $pO_2 \approx 10^{-14}$ atm, and oxygen is absent when methane is injected, it is safe to say the participation of oxygen in activation of methane is negligible. The absence of H₂O from the second pulse suggests the absence of OH*-group-producing processes on the nickel surface, as H₂O is mainly produced via: $OH^* + H^* \rightarrow H_2O^*$ or $OH^* + OH^* \rightarrow H_2O^* + H^*$ [49]. This suggests in the POM at given conditions, the oxygen from CGO participates in the reaction only by oxidizing carbon species on Ni.

3.3. Carbon deposition and reoxidation of CGO

It is also possible to reoxidise the CGO in between pulses of methane, using pulses of 12.3% steam. To avoid the influence of carbon deposition, a smaller loop size is used. Seven methane pulses of 0.2326 mL (equivalent to 103.8 μmol/g CH₄) were injected at 600 °C with 20 min interval in each cycle. Similar steam pulses performed on nickel powder of 50 nm particle size did not show noticeable nickel oxidation, suggesting that it can be assumed that only CGO was oxidized in the steam pulse. Pulses of 12.3% steam/Ar mixing gas is injected to the sample and produced only hydrogen. CO production peaks of the first cycle are shown in Fig. 4b, and the integrated production amount is concluded in Fig. 4c. The CO production amount is constant in the second to sixth pulse in a cycle despite the shape change, which is consistent with previous observations, and steam pulses are able to fully

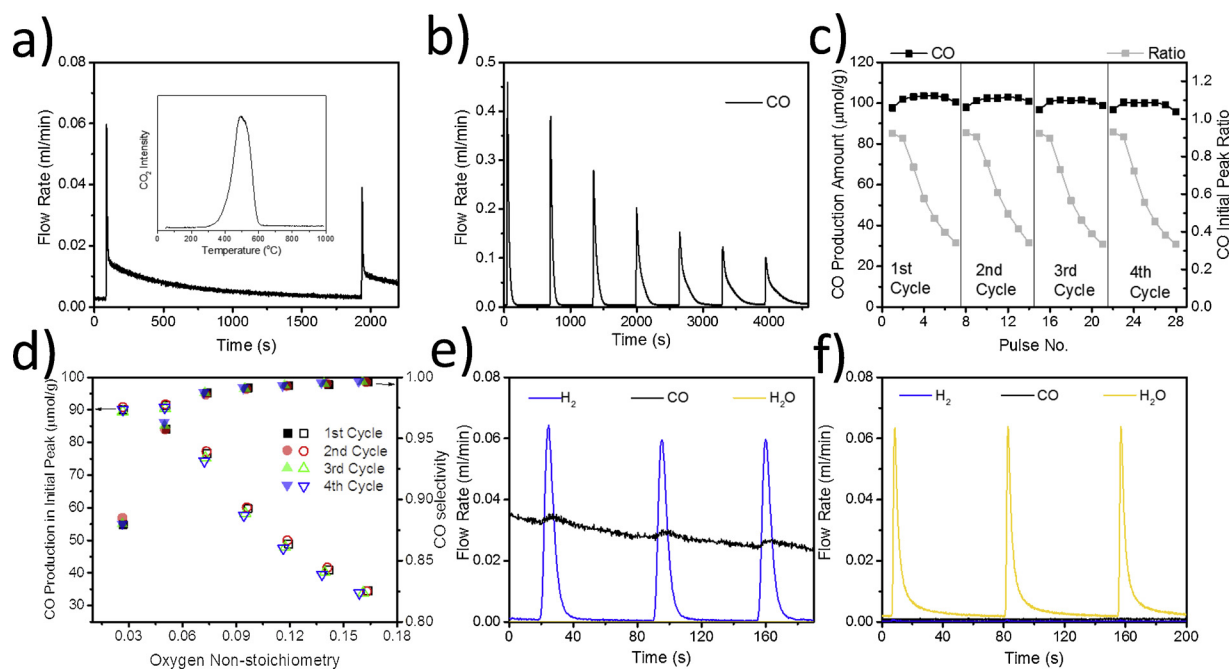


Fig. 4. Carbon deposition and CGO reoxidation a) An excerpt from the CO production of methane pulse with 30 min interval, showing the CO production from the fifth methane pulse. It indicates the overlaps of the CO tail with the sixth pulse, inset is the temperature programmed oxidation after the methane pulse with 30 min interval indicated by CO₂ production. b) CO production in the first cycle of methane pulse with steam reoxidation; c) The CO production amount and ratio of initial peak in methane pulse with water oxidation experiment. The black line is the CO production amount in each methane pulse; the grey line is the proportion of CO produced in the initial peak versus the total CO production in each pulse. d) CO production amount in the initial peak and selectivity towards POM plotted with changing oxygen non-stoichiometry in four cycles of methane pulse with water reoxidation; e) An excerpt from water pulse oxidation on Ni/CGO after methane pulses when CO is still emerging at the tail. All water was converted to hydrogen and that the rate of CO oxidation was enhanced.; f) An excerpt from water pulse oxidation on Ni/YSZ after methane pulses. In the methane pulse with water re-oxidation experiment 12.3% water/Ar pulses were injected every seven pulses of methane until no hydrogen is produced.

reoxidise the sample to its initial state, as evidenced by the fact that CO production in all four cycles are identical with each other (Fig. 4c). The methane pulse features recover at the start of each cycle, suggesting that the CGO oxidation state is the determining factor in the carbon oxidation rate.

Oxygen non-stoichiometry δ after each pulse relative to the initial oxidation state of CGO at the start of each cycle is calculated by CO and CO₂ production. As shown in Fig. 4d, the selectivity towards POM in all four cycles followed the same trend as a function of oxygen non-stoichiometry of CGO, which is over 85% at $\delta = 0.027$, and further increases to > 99% at $\delta = 0.073$. Indicating the selectivity of methane oxidation is closely related with oxidation state of CGO, a high selectivity towards POM can be achieved by slightly increasing the oxygen non-stoichiometry of CGO and maintaining oxygen supply by steam. Therefore, while oxygen often over-oxides the metal compound in catalysts, making it prone towards TOM [50], steam, and potentially CO₂ as they share similar oxidation ability towards CGO, can be used in methane CLR for controlling of CGO oxidation state for high POM selectivity.

The CO production amount in the initial peak as a function of CGO non-stoichiometry also showed good reproducibility for all cycles. According to the mechanism deduced previously, the CO production amount in the initial peak indicates oxygen on the surface of CGO that is consumable by oxidation of carbon species. The oxygen consumption in the first initial peak of each cycle is ~90 μmol/g, equivalent to two oxygen monolayers on CGO, calculated using the condition of full oxygen stoichiometry (Gd_{0.1}Ce_{0.9}O_{1.95}), and specific surface area of 100 μm²/μm³. On the other hand, using the total reducible oxygen (~830 μmol/g) and reducible surface oxygen ratio at 100 nm (~10%) from Xu's work [51], the estimated reducible surface oxygen at full oxidation state of CGO is 83 μmol/g, which is in good accordance with our experiment data. This in turn adds to the credibility of our proposed

mechanism.

Some literature suggests that the metal sites at the metal-CGO interface are more active because the adsorbed species would dissociate faster at the interface due to formation of bridging bonds of adsorbed species ($-\text{CH}_4$) with metal and oxygen ions on the support [30,35,52], therefore, such an effect is closely related to the concentration of surface oxygen vacancies [53]; However, here it was found that the production of CO and consumption of methane of each cycle did not change with decreasing CGO oxidation state, which suggestss the activation of methane is not affected by the oxygen concentration on the CGO surface. Such irrelevance has also been found by Wei [54], who concluded the support is not involved in the activation of methane. Also, if we consider a nickel surface site density of $3.3 \times 10^{-3} \mu\text{mol}/\text{cm}^2$ [55], and nickel average diameter of 20 nm, assuming the nickel particles are all in hemispheric, the concentration of gravimetric surface sites on the nickel surface is then 91.9 μmol/g, which is slightly smaller than the CO production in each methane pulse. However, the concentration of perimeter sites is 2.3 μmol/g, which is too small for the amount of methane consumed. It is still difficult to conclude that methane does not preferably activate on the perimeter, but it is safe to say that in this condition the top of nickel also contributes significantly to the activation of methane. However the high activity of metal-oxide interface has been well accepted in the field of catalysis, the reason it is not significant here is probably: 1. The nickel particle size in this work (~20 nm) is not small enough to give a high perimeter/surface ratio; 2. In the given oxygen free condition, there is already a high concentration of oxygen vacancies on the surface of CGO, so the decrease of oxygen concentration at the interface is not significant during the methane pulse.

If the steam pulse is introduced while there is still CO being produced (Fig. 4e), the observation is that there is a spike of hydrogen and an increase in the rate of CO production concomitant with an increase

in the oxidation state of the CGO. Parallel experiments on Ni/YSZ after methane pulses did not show similar hydrogen peaks and increment of CO (Fig. 4f). The results are consistent with the steam reacting exclusively with the CGO, and not with the carbonaceous species present on the surface of the nickel. The increasing of CGO oxidation state in turn enhance the carbon oxidation rate. This shows that even when steam is present to react with carbon species on the nickel, the reaction still proceeds via the Mars-van Krevelen mechanism, with oxygen migration being the rate limiting step.

3.4. Discussion and implications

The results indicate that the rates of carbon oxidation by oxygen on nickel, the spill-over of oxygen onto nickel, and the surface transport of oxygen on CGO are rapid compared to the bulk transport of oxygen in CGO, and this has different consequences for catalysts compared to SOFC anodes. In SOFC anodes, methane is continuously supplied, and the oxygen is always supplied from the bulk of the oxygen-conducting phase, so the rate of methane oxidation will be limited by the rate of oxygen transport through the bulk. The activation of methane, however, is determined by the surface area of nickel. Therefore, to mitigate carbon deposition in SOFCs, the rate of methane activation needs to be smaller than the carbon oxidation. In other words, the surface area of nickel needs to be matched to the thermodynamic equilibrium of the system and the structure of the CGO support.

In contrast, in methane CLR, the catalyst is replenished in the oxidizing chamber after reacting with methane, so minor carbon deposition is not a problem as long as it does not damage the catalyst structure. However, selectivity towards POM is crucial for efficient syngas production [11]. Here it is demonstrated that desired POM selectivity can be acquired by controlling the CGO oxidation state in a certain range. TOM will occur if the oxidation state is too high, and carbon deposition will accumulate if too low. Our results also show that the quantity of oxygen available for the rapid surface oxygen transport is relatively limited, and will decrease as the CGO becomes more reduced. This can be fully replenished by low concentration of steam without significant oxidation of nickel, which happens when oxygen is used to replenish the catalyst. This implies that to acquire high selectivity and mitigate carbon deposition, it is important to control the CGO oxidation state by adjusting the time and amount of methane and steam reactant in the reaction-oxidation cycle of CLR.

The methane pulse experiment used in this work has proven to be a facile and useful tool to analyse the catalytic properties of heterogeneous catalysts, especially those reactions that contain various steps with different rates, such as the oxidation of methane. Abundant qualitative information has been extracted from the result by simply analysing the shape and broadening of peaks. It can also potentially provide access to quantitative information linked with intrinsic properties of heterogeneous catalysts. As an example, the diffusion coefficient and diffusion distance of CGO with different oxidation states can potentially be extracted from the fitting of the decay of the CO tail. Together with the carbon deposition amount and carbon oxidation rate, which can already be extracted from our experiment data, the carbon resistivity of catalysts can be evaluated comprehensively. Future work will focus on extracting further quantitative information from methane pulse experiments and to set up an objective way to evaluate the performance of heterogeneous catalysts.

4. Conclusions

To summarise, we have applied facile methane pulse experiments on a Ni impregnated CGO powder catalyst to investigate the reaction of methane in oxygen free conditions. By analysing the shape of peaks and the production amount of species, following conclusions were drawn:

1 Partial oxidation of methane on Ni/CGO catalyst goes through a

Mars van-Krevelen type mechanism, in which methane is first activated on nickel, forming carbon species (CH_x^*) and then oxidized by oxygen migrated from CGO. Total oxidation of methane only happens when the CGO oxidation state is high, and likely involves oxygen adsorbed on nickel. Nickel has no appreciable solubility in CGO [56] so the presence of Ni in the CGO lattice was discounted:

- a The activation of methane is not affected by the CGO oxidation state. All the surface of nickel contributes to the activation of methane.
- b There are two oxidation stages of carbon species: the first is oxidation by surface oxygen of CGO, the second is by the oxygen migrated from the bulk CGO after surface oxygen is depleted. The rate limiting step of the second oxidation process is the oxygen migration from bulk to surface of CGO, whose rate decreases with increasing oxygen non-stoichiometry of CGO.

2 The highly amorphous carbon deposition after methane pulse deactivates the catalyst by blocking the active sites on nickel surface, and can be eliminated by oxygen from CGO, if enough time is allowed for the migration of oxygen from bulk.

3 The oxygen migration and POM selectivity is closely related with the oxidation state of CGO. Low concentrations of steam can replenish the oxidation state of CGO without significant oxidation of nickel and thus can be used to control the oxidation state.

Acknowledgements

The authors acknowledge support from EPSRC grants EP/M02346X/1 and EP/P024807/1, and the China Scholarship Council, and by the EPSRC energy storage for low carbon grids project (EP/K002252/1), the EPSRC Joint UK-India Clean Energy centre (JUICE) (EP/P003605/1).

Appendix A. Supplementary data

Supplementary material related to this article can be found, in the online version, at doi:<https://doi.org/10.1016/j.apcatb.2019.02.038>.

References

- [1] S. McIntosh, R.J. Gorte, Direct hydrocarbon solid oxide fuel cells, *Chem. Rev.* 104 (10) (2004) 4845–4866.
- [2] A. Haryanto, et al., Current status of hydrogen production techniques by steam reforming of ethanol: a review, *Energy Fuels* 19 (5) (2005) 2098–2106.
- [3] F. Pompeo, G. Santori, N.N. Nichio, Hydrogen and/or syngas from steam reforming of glycerol. Study of platinum catalysts, *Int. J. Hydrogen Energy* 35 (17) (2010) 8912–8920.
- [4] J.A. Velasco, et al., Catalytic partial oxidation of methane over nickel and ruthenium based catalysts under low O₂/CH₄ ratios and with addition of steam, *Fuel* 153 (2015) 192–201.
- [5] S. Prukshawan, B. Kitiyanan, R.M. Ziff, Partial oxidation of methane on a nickel catalyst: kinetic Monte-Carlo simulation study, *Chem. Eng. Sci.* 147 (2016) 128–136.
- [6] A. Thallam Thattai, L. van Biert, P.V. Aravind, On direct internal methane steam reforming kinetics in operating solid oxide fuel cells with nickel-ceria anodes, *J. Power Sources* 370 (2017) 71–86.
- [7] M.D. Gross, J.M. Voehs, R.J. Gorte, Recent progress in SOFC anodes for direct utilization of hydrocarbons, *J. Mater. Chem.* 17 (30) (2007) 3071–3077.
- [8] P. Boldrin, et al., Strategies for carbon and sulfur tolerant solid oxide fuel cell materials, incorporating lessons from heterogeneous catalysis, *Chem. Rev.* 116 (22) (2016) 13633–13684.
- [9] D.A. Andersson, et al., Optimization of ionic conductivity in doped ceria, *Proc. Natl. Acad. Sci. U. S. A.* 103 (10) (2006) 3518–3521.
- [10] S.P.S. Badwal, et al., Structural and microstructural stability of ceria - gadolinia electrolyte exposed to reducing environments of high temperature fuel cells, *J. Mater. Chem. A* 1 (36) (2013) 10768–10782.
- [11] A. Löfberg, et al., Ni/CeO₂ based catalysts as oxygen vectors for the chemical looping dry reforming of methane for syngas production, *Appl. Catal. B* 212 (2017) 159–174.
- [12] A. Hedayati, et al., Evaluation of novel ceria-supported metal oxides as oxygen carriers for chemical-looping combustion, *Ind. Eng. Chem. Res.* 51 (39) (2012) 12796–12806.
- [13] L. Maier, et al., Steam reforming of methane over nickel: development of a multi-step surface reaction mechanism, *Top. Catal.* 54 (13) (2011) 845.
- [14] M. Cargnello, et al., Control of metal nanocrystal size reveals metal-support

interface role for ceria catalysts, *Science* 341 (6147) (2013) 771–773.

[15] H.A.E. Dole, et al., Quantifying metal support interaction in ceria-supported Pt, PtSn and Ru nanoparticles using electrochemical technique, *J. Catal.* 333 (2016) 40–50.

[16] R.C. Maher, et al., Reduction dynamics of doped ceria, nickel oxide, and cermet composites probed using *in situ* Raman spectroscopy, *Adv. Sci.* 3 (1) (2016) 1500146 n/a.

[17] Z. Liu, et al., *In situ* investigation of methane dry reforming on metal/ceria(111) surfaces: metal–support interactions and C–H bond activation at low temperature, *Angew. Chemie Int. Ed.* 56 (42) (2017) 13041–13046.

[18] J.T. Gleaves, et al., Temporal analysis of products (TAP)—recent advances in technology for kinetic analysis of multi-component catalysts, *J. Mol. Catal. A Chem.* 315 (2) (2010) 108–134.

[19] K. Morgan, et al., Forty years of temporal analysis of products, *Catal. Sci. Technol.* 7 (12) (2017) 2416–2439.

[20] V. Balcaen, et al., TAP study on the active oxygen species in the total oxidation of propane over a Cu0–CeO2/γ-Al2O3 catalyst, *Catal. Today* 157 (1) (2010) 49–54.

[21] Z. Song, W. Liu, H. Nishiguchi, Quantitative analyses of oxygen release/storage and CO₂ adsorption on ceria and Pt–Rh/ceria, *Catal. Commun.* 8 (4) (2007) 725–730.

[22] O. Dewaele, G.F. Froment, TAP study of the mechanism and kinetics of the adsorption and combustion of methane on Ni/Al2O3 and NiO/Al2O3, *J. Catal.* 184 (2) (1999) 499–513.

[23] R.B. Duarte, et al., Transient mechanistic studies of methane steam reforming over ceria-promoted Rh/Al2O3 catalysts, *ChemCatChem* 6 (10) (2014) 2898–2903.

[24] C.B. Gopal, S.M. Haile, An electrical conductivity relaxation study of oxygen transport in samarium doped ceria, *J. Mater. Chem. A* 2 (7) (2014) 2405–2417.

[25] A. Falkenstein, et al., Chemical relaxation experiments on mixed conducting oxides with large stoichiometry deviations, *Solid State Ion.* 280 (2015) 66–73.

[26] M. Katsuki, et al., The oxygen transport in Gd-doped ceria, *Solid State Ion.* 154–155 (2002) 589–595.

[27] K. Yashiro, et al., Mass transport properties of Ce0.9Gd0.1O₂–8 at the surface and in the bulk, *Solid State Ion.* 152–153 (2002) 469–476.

[28] G.A. Somorjai, et al., The evolution of model catalytic systems; studies of structure, bonding and dynamics from single crystal metal surfaces to nanoparticles, and from low pressure (< 10–3 Torr) to high pressure (> 10–3 Torr) to liquid interfaces, *Phys. Chem. Chem. Phys.* 9 (27) (2007) 3500–3513.

[29] V.A. Sadykov, et al., Partial oxidation of methane on Pt-supported lanthanide doped ceria-zirconia oxides: effect of the surface/lattice oxygen mobility on catalytic performance, *Catal. Today* 169 (1) (2011) 125–137.

[30] A. Ruiz Puigdollers, et al., Increasing oxide reducibility: the role of metal/oxide interfaces in the formation of oxygen vacancies, *ACS Catal.* 7 (10) (2017) 6493–6513.

[31] M.Y. Smirnov, G.W. Graham, Pd oxidation under UHV in a model Pd/ceria–zirconia catalyst, *Catal. Letters* 72 (1) (2001) 39–44.

[32] G.S. Zafiris, R.J. Gorte, Evidence for low-temperature oxygen migration from ceria to Rh, *J. Catal.* 139 (2) (1993) 561–567.

[33] G.N. Vayssilov, et al., Support nanostructure boosts oxygen transfer to catalytically active platinum nanoparticles, *Nat. Mater.* 10 (4) (2011) 310–315.

[34] Y.-H. Chin, et al., Reactivity of chemisorbed oxygen atoms and their catalytic consequences during CH₄–O₂ catalysis on supported Pt clusters, *J. Am. Chem. Soc.* 133 (40) (2011) 15958–15978.

[35] G.N. Vayssilov, et al., Support nanostructure boosts oxygen transfer to catalytically active platinum nanoparticles, *Nat. Mater.* 10 (2011) 310.

[36] T. Skalar, et al., Oxidation of carbon deposits on anode material Ni–YSZ in solid oxide fuel cells, *J. Therm. Anal. Calorim.* 127 (1) (2017) 265–271.

[37] S. Hofmann, et al., In situ observations of catalyst dynamics during surface-bound carbon nanotube nucleation, *Nano Lett.* 7 (3) (2007) 602–608.

[38] I.P. Silverwood, et al., Quantification of surface species present on a nickel/alumina methane reforming catalyst, *Phys. Chem. Chem. Phys.* 12 (13) (2010) 3102–3107.

[39] M. Audier, et al., Morphology and crystalline order in catalytic carbons, *Carbon* 19 (3) (1981) 217–224.

[40] Z.-Y. Pu, et al., Study of oxygen vacancies in Ce0.9Pr0.1O₂–8 solid solution by *in situ* X-ray diffraction and *in situ* Raman spectroscopy, *J. Phys. Chem. C* 111 (50) (2007) 18695–18702.

[41] J.R. McBride, et al., Raman and x-ray studies of Ce1–xRExO2–y, where RE=La, Pr, Nd, Eu, Gd, and Tb, *J. Appl. Phys.* 76 (4) (1994) 2435–2441.

[42] N. Mironova-Ulmane, et al., Raman scattering in nanosized nickel oxide NiO, *J. Phys. Conf. Ser.* 93 (1) (2007) 012039.

[43] V. Duboviks, et al., A Raman spectroscopic study of the carbon deposition mechanism on Ni/CGO electrodes during CO/CO₂ electrolysis, *Phys. Chem. Chem. Phys.* 16 (26) (2014) 13063–13068.

[44] A.C. Ferrari, et al., Raman Spectrum of graphene and graphene layers, *Phys. Rev. Lett.* 97 (18) (2006) 187401.

[45] C.S. Feigerle, S.R. Desai, S.H. Overbury, The kinetics of CO desorption from Ni (110), *J. Chem. Phys.* 93 (1) (1990) 787–794.

[46] I. Chorkendorff, J.N. Russell, J.T. Yates, Hydrogen implantation in Ni(111) — a study of H₂ desorption dynamics from the bulk, *Surf. Sci.* 182 (3) (1987) 375–389.

[47] A. Holmgren, D. Duprez, B. Andersson, A model of oxygen transport in Pt/ceria catalysts from isotope exchange, *J. Catal.* 182 (2) (1999) 441–448.

[48] X.-B. Ren, H.-Y. Li, X.-Y. Guo, Monte Carlo simulation of the oscillatory behavior in partial oxidation of methane on nickel catalyst, *Surf. Sci.* 602 (1) (2008) 300–306.

[49] M. Jørgensen, H. Grönbeck, First-principles microkinetic modeling of methane oxidation over Pd(100) and Pd(111), *ACS Catal.* 6 (10) (2016) 6730–6738.

[50] S. Bhavar, G. Veser, Reducible supports for Ni-based oxygen carriers in chemical looping combustion, *Energy Fuels* 27 (4) (2013) 2073–2084.

[51] J. Xu, et al., Size dependent oxygen buffering capacity of ceria nanocrystals, *Chem. Commun.* 46 (11) (2010) 1887–1889.

[52] M. Ichikawa, T. Fukushima, Infrared studies of metal additive effects on carbon monoxide chemisorption modes on silicon dioxide-supported rhodium-manganese-, titanium and iron catalysts, *J. Phys. Chem.* 89 (9) (1985) 1564–1567.

[53] A. Boffa, A. Bell, G. Somorjai, Vanadium oxide deposited on an Rh foil: CO and CO₂ hydrogenation reactivity, *J. Catal.* 139 (2) (1993) 602–610.

[54] J. Wei, E. Iglesia, Mechanism and site requirements for activation and chemical conversion of methane on supported Pt clusters and turnover rate comparisons among noble metals, *J. Phys. Chem. B* 108 (13) (2004) 4094–4103.

[55] K. Christmann, O. Schober, G. Ertl, Adsorption of CO on a Ni(111) surface, *J. Chem. Phys.* 60 (12) (1974) 4719–4724.

[56] P. Datta, P. Majewski, F. Aldinger, Synthesis and reactivity study of gadolinia doped ceria-nickel: a potential anode material for solid oxide fuel cell, *J. Alloys. Compd.* 455 (1) (2008) 454–460.